Helium and Strontium co-implantation into SiC at Room Temperature and Isochronal Annealing: Structural Evolution of SiC and Migration Behaviour of Strontium

Thapelo Mokgadi[a,*], Zaki Abdalla[a], Hesham Abdelbagi[a], Mandla Msimanga[b,c], Charity Maepa[a], Vladimir Skuratov[d,e,f], Thulani Hlatshwayo[a]

[a] Physics Department, University of Pretoria, Private Bag X20, 0028 Hatfield, South Africa

[b] Physics Department, Tshwane University of Technology, Private Bag X680, Pretoria, 0001, South Africa

[c] iThemba LABS TAMS, National Research Foundation, Private Bag 11, WITS 2050, Johannesburg, South Africa

[d] Joint Institute for Nuclear Research, Dubna, Russia

[e] National Research Nuclear University MEPhI, Moscow

[f] Dubna State University, Dubna, Moscow Region, Russia

*Corresponding author. E-mail address: tf.mokgadi@up.ac.za (Thapelo Mokgadi)

Highlights

- After implantation, an amorphous layer is formed.
- Recrystallization occurred after annealing.
- After annealing at high temperatures, He exo-diffused through the free surface.
- He-induced defects (cavities) represents the center of trapping of Sr atoms.

Abstract

Understanding the structural evolution of SiC implanted with fission product surrogates in the presence of helium (He) is of importance for its application in both fission and fusion rectors. In this study, polycrystalline SiC wafers were sequentially co-implanted with 360 keV Sr and 21.5 keV He ions to a fluence of 2×10^{16} cm^{-2} and 1×10^{17} cm^{-2} at room temperature, respectively. The samples were then isochronally annealed in temperatures ranging from 1000 to 1300 ºC for 5 h. Transmission electron microscopy (TEM) showed the formation of He-nanobubbles corresponding to helium's projected range. While scanning electron microscopy (SEM) revealed the formation of cornflower-like structures on the surface of the Sr+He-SiC samples after annealing. These were confirmed to be holes by atomic force microscopy (AFM), as a result of exfoliation and pressurized out-diffusion of helium gas from the samples. The Sr+He-SiC samples were completely amorphized characterized by the formation of the

homonuclear bonds in Raman spectroscopy. The recovery process after annealing in the Sr+He-SiC samples resulted in the formation of graphite due to antisite defects driven by the growth of holes above the threshold chemical disorder. Time-of-flight heavy ions elastic recoil detection analysis (Tof-ERDA) showed that almost all helium out-diffused after annealing at 1000 ºC and Sr atoms trapped in He cavities.

Graphical abstract

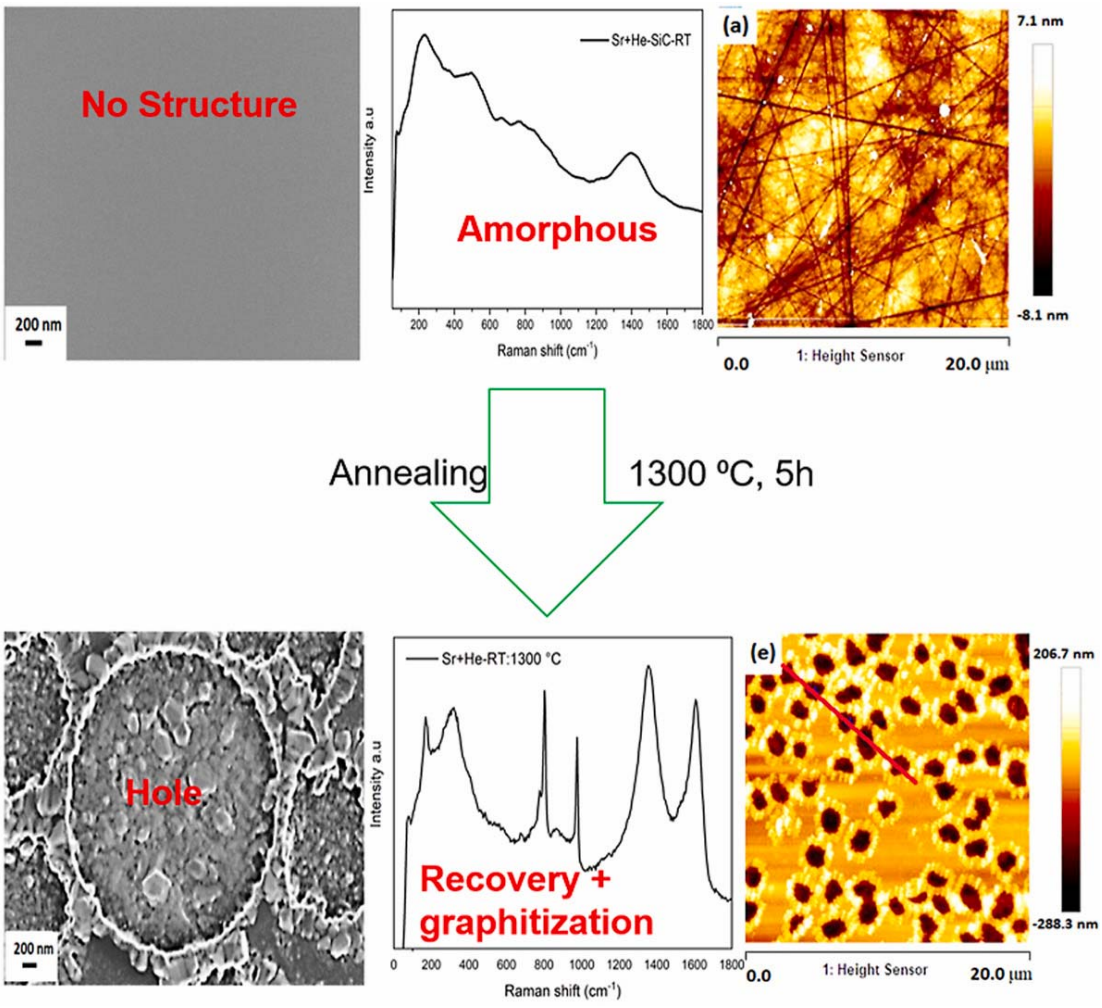

Keywords: AFM, Chemical disorder, Graphitization, Helium, surface-parallel nanobubbles

1. Introduction

Silicon carbide (SiC) has found use in a wide range of applications over the years. Owing to its high breakdown voltage, higher saturated electron drift velocity and higher thermal conductivity, it has been employed as a large-bandgap semiconductor in very harsh environments such as power electronics, ultraviolet (UV) sensors, and micro-electro-mechanical systems (MEMS) [1, 2]. Not only is it an exceptionally good semiconductor, it can also be engineered into a single-photon solid state source with a wide emission range for applications in quantum technologies [3–5]. Furthermore, the need to develop materials that are structurally and mechanically stable up to high temperatures and ones that can withstand the extreme nuclear environments has led to the investigations of SiC as a suitable candidate for both fission and fusion reactors [6, 7]. Of interest in the nuclear environment are its creep and oxidation resistance [8–10], radiation tolerance [11–14], low neutron capture cross section [15], low radioactivity [16] and perfect chemical stability [17].

SiC is used as a structural material in fusion reactors and as a main diffusion barrier of fission products in modern generation IV reactors. In both reactors, SiC is subjected to ion and neutron irradiations of different energies in the presence of helium (He) from actinide radioactive decay and nuclide transmutation [18]. Helium is known to form bubbles in SiC at low irradiation temperature (less than 600 °C) [16,17,19-29], and He atoms are trapped into platelets for high irradiation temperature [29, 30].The formation of bubbles induces deleterious effects on the physical integrity of SiC (e.g., formation of cracks, surface swelling and exfoliation) vital in the nuclear context [2,17,19-22]. These bubbles are formed as a result of migration and agglomeration of He atoms and vacancies at high temperatures due to low solubility of He in materials [23-28]. The presence of bubbles limits the migration of Frenkel pairs, dislocation loops, and stacking faults, thus weakening the mechanical properties of materials [31-34]. Helium bubbles in SiC are estimated to form after irradiation to a fluence of 10^{17} cm^{-2} with a threshold concentration of about 4.0 at. %, while a significant amount of He is released during implantation to a fluence of 10^{18} cm^{-2} [35]. The He bubbles grow substantially after annealing at 1200 ºC, with the bubble layer becoming more carbon enriched due to long dislocations being transformed into dislocation channels as reported by Li et al. [36].

To fully understand the role of He in the structural evolution of SiC in nuclear reactors, one needs to understand the structural evolution of SiC in the presence of fission products, neutrons and He at elevated temperatures. Recently, krypton (Kr) co-implanted with He in 3C-SiC [37]

has been investigated, and the presence of He was found to cause larger cavities, while smaller cavities were observed in the Kr only implanted SiC at the same fluence. This caused Kr atoms to migrate towards the He cavities and being trapped in cavities. In another study, co-implantation of Ag and He at room temperature resulted in a cavity network parallel to the surface after annealing at 1100 ºC causing a segregation of Ag around the cavity network [38]. The effects of He-induced defects (cavities) in Fe and He co-implanted SiC at room temperature has also been studied [39]. The study reported on Fe atoms being trapped in cavities causing large Fe clusters after annealing at 1500 °C. A different sudy with similar irradiation conditions was also done looking at the chemical disorder after annealing [40]. The study also found that He-induced cavities were created and the electrcon energy-loss spectroscopy (EELS) analysis found that within the cavities were lower Si at. % and higher C and O at. %. However, there are still questions to be answered about the role of bubbles and their rupture (cavities) in the structural modification and migration of the implanted fission products. In this study we report on the microstructural evolution and migration in polycrystalline SiC co-implanted with He and strontium (Sr) at room temperature and post-irradiation heat treatments. Specifically, ^{90}Sr is a radiobiological medium-lived fission product with about 6% yield in the U-235 fuel and has a half-life of about 29 years. It mimics calcium and can deposit in bones and teeth causing cancers. Moreover, Sr is one of the radiologically important fission products that has been reported to migrate through SiC during operation [41] and to the best of our knowledge the influence of He bubbles in the migration of Sr has not been investigated.

2. Experimental Method

Polycrystalline SiC wafers from Valley Design Corporation were used in this study. Before implantation, the wafers were characterized by X-ray diffraction (XRD), Raman spectroscopy and electron backscatter diffraction (EBSD) [42-44]. They were found to be mainly composed of 3C-SiC with some traces of 6H-SiC. The wafers were implanted with Sr ions of 360 keV to a fluence of 2×10^{16} cm^{-2} at room temperature (RT), under vacuum at the Friedrich-Schiller-University in Jena, Germany. Some of the Sr implanted samples were then implanted with helium (He) ions of 21.5 keV (to allow for the overlap of the Sr and He profiles) to a fluence of 1×10^{17} cm^{-2} at RT. The He implantation was performed at the tandem and accelerator mass spectrometry (TAMS) Laboratory, iThemba LABS, Johannesburg, South Africa. Both the Sr implanted (Sr-SiC) and Sr and He co-implanted (Sr+He-SiC) samples were isochronally

annealed at 1000, 1100, 1200 and 1300 ºC for 5 h under vacuum (10^{-5} Pa). The as-implanted and annealed Sr-SiC samples were characterized by transmission electron microscopy (TEM), scanning electron microscopy (SEM), Raman spectroscopy and time-of-flight heavy elastic recoil detection analysis (ToF-ERDA), while the as-implanted and annealed Sr+He-SiC samples were additionally characterized by atomic force microscopy (AFM).

The computer-controlled *Webb* graphite furnace was used to isochronally anneal the samples at temperatures from 1000 to 1300 ºC in steps of 100 ºC for 5 h. TEM was performed on the as-implanted and 1000 ºC annealed Sr-SiC and Sr+He-SiC samples. TEM lamellas were prepared by focussed ion beam (FIB) technique using a *FEI Helios Nanolab 650* FIB. Thinning of the samples was performed by successive 30 keV and 5 keV Ga ions. Finally, polishing was done at 2 keV and 500 eV which produced near damage free TEM foils. TEM analysis was then performed using the *JEOL JEM 2100F* field emission transmission electron microscope operating at 200 kV.

The surface morphological evolution of Sr-SiC and Sr+He-SiC samples were monitored before and after annealing using *Zeiss Gemini Ultra Plus* field emission gun scanning electron microscopy (FEG-SEM). The in-lens detector and accelerating voltage of 2 kV were used. Single spectra Raman spectroscopy measurements were performed on the Sr-SiC and Sr+He-SiC samples before and after annealing using the *Witec alpha 300 RAS+* Raman spectrometer. Data acquisition was carried out using the 532 nm excitation laser wavelength, 5 mW laser power, and 100×/0.9 numeric aperture objective. The surface morphology of the Sr+He-SiC samples before and after annealing were also characterized using the *Bruker Dimension Icon* with ScanAsyst AFM system in air mode. AFM micrographs were analysed using the *NanoScope* Analysis software over the scan area of 20 µm × 20 µm. The as-implanted and samples annealed at 1000 ºC were analysed by ToF-ERDA at TAMS Laboratory, iThemba LABS, Johannesburg, South Africa, using 20 MeV $^{197}Au^{6+}$ ions produced by a 6-MV Tandem accelerator. The heavy ion ToF-ERDA setup consists of a mass dispersive ToF spectrometer having two carbon foil based Microchannel Plate (MCP) time detectors. The two detectors are 0.6 m apart and the setup also consists of a passivated implanted planar silicon (PIPS) energy detector at the end of the flight path behind the second time detector. The spectrometer is located at 30° to the direction of the incident beam, while the target is tilted 15° to the direction of the incident beam. More details of the ToF-ERDA set-up can be found elsewhere [45]. The analysis was undertaken with the Potku data analysis program [46].

The concentration distribution and lattice damage of Sr (360 keV) and He (21.5 keV) ions implanted into SiC were simulated by the stopping and range of ions in matter (SRIM) 2013 [47] software. The detailed calculation with full damage cascades was used with the density of 3.21 gcm^{-3} for SiC and the threshold displacement energies of 35 and 20 eV for Si and C, respectively. Fig.1 shows the simulated concentration distribution of Sr and He, the simulated lattice damage in dpa of Sr, He and the total dpa in the Sr+He-SiC sample. Sr implantation resulted in a depth profile with a projected range (Rp) of about 140 nm and a maximum relative atomic density of 2.26 at. %, while the maximum lattice damage of about 2.60 dpa was retained at a depth of 110 nm. He implantation resulted in a He profile with a Rp of about 150 nm and maximum relative atomic density of about 12 at. %, while the maximum dpa of about 1.93 was retained at a depth of 130 nm. The total maximum dpa in the Sr+He samples of about 4.40 dpa at a depth of 110 nm was retained. From these simulated results it is quite clear that the Sr and He profiles overlap which allows the investigation of their synergy in the structural evolution of SiC and the role of He bubbles in the migration of Sr. Moreover, there are more damage in the Sr+He-SiC sample compared to individually implanted samples owing to the interaction of defects in the Sr+He-SiC samples. If 0.3 dpa is needed to amorphize SiC [48], about 202 nm of SiC layer will be amorphized by Sr ions only and about 198 nm will be amorphized by the He ions only, while about 211 nm will be amorphized by the total contribution in the co-implanted SiC.

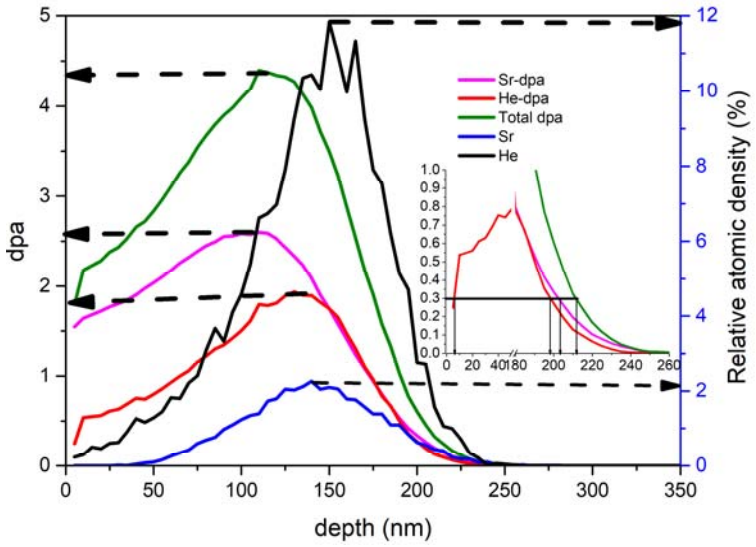

Fig 1. *Relative atomic density, and displacement per atom (dpa) from TRIM simulation calculations of Sr and He ions implanted SiC. Insert shows the depth at 0.3 dpa for He, Sr and the total contribution.*

3. Results and Discussion

The bright field TEM micrographs of as-implanted Sr-SiC and Sr+He-SiC samples are shown in Fig. 2, where they are overlayed with SRIM simulated results. In both micrographs bulk is indicated by double arrows while the surface is indicated by a blue arrow in Fig. 2 (a) and (c). Single implantation of Sr resulted in an amorphous layer of about 250 nm (shown in Fig. 2 (a)) thickness, while co-implantation of He resulted in an increase of amorphous layer to about 300 nm (shown in Fig. 2(c)) accompanied by the formation of nanobubbles in the region from 25 nm to about 150 nm below the surface. The observed added swelling is due to the decrease in density induced by further amorphization [49]. Similar formation of He nano-bubbles accompanied by swelling have been reported for He implanted into the silver pre-implanted polycrystalline SiC to a fluence of 1×10^{17} cm^{-2} at RT [38]. Moreover, it has been previously reported that only helium bubbles of about 1 nm in diameter can be formed from He ion implantation into SiC to fluences between 1.5×10^{16} and 1.0×10^{17} cm^{-2} [50], which is consistent with our findings.

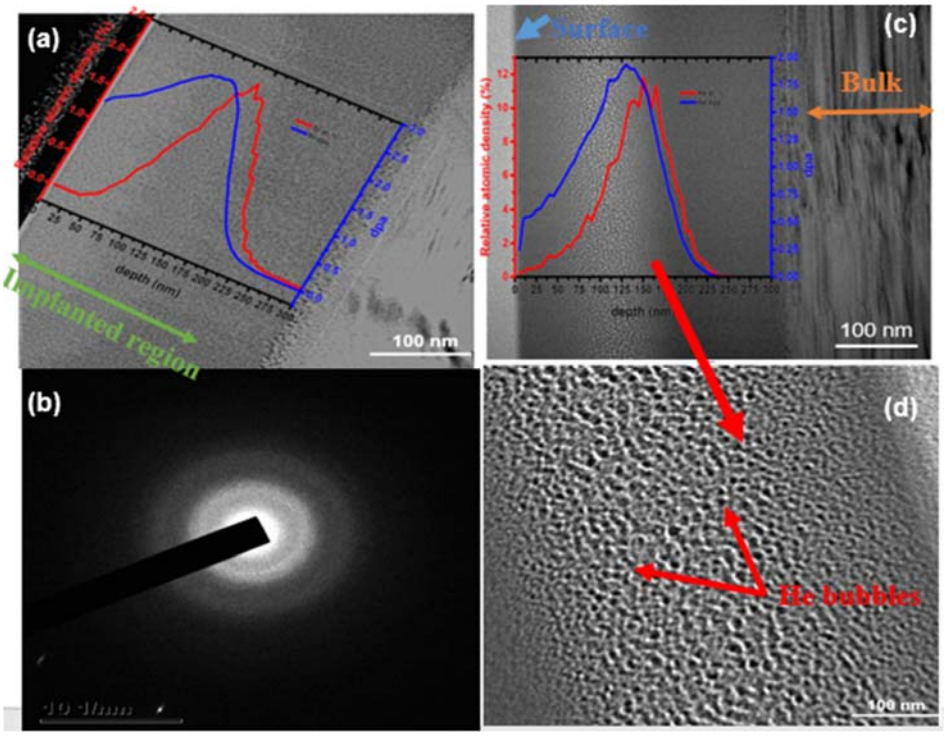

Fig. 2. *Bright field (BF) TEM micrographs of (a) Sr as-implanted SiC at room temperature. (b) Selected area difraction (SAD) of the implanted region of (a), (c) Sr & He as-implanted also at room temperature. Both micrographs are overlayed with their respective SRIM simulated results. Double arrows indicate the bulk while blue arrows indicate the surface. (d) Detailed bubbles in the amorphous layer of Sr+He-SiC at higher magnification.*

The structural evolutions of as implanted and annealed samples were investigated using Raman spectroscopy. Fig. 3 shows the Raman spectrum of the pristine SiC with the insert showing the magnified region (1000 – 2000 cm^{-1}). Raman spectrum of pristine SiC shows the characteristic Raman peaks with a sharp longitudinal optical (LO) mode at 972 cm^{-1} and the transverse optical (TO) mode which is normally Raman inactive in the backscattering mode [51], at 801 cm^{-1} as have been shown elsewhere [52,53]. The transverse optical mode appearing at 776 cm^{-1} belongs to the 6H-SiC polytype [54], which agrees with previous Raman and EBSD studies [42-44,55]. The higher wavenumber region shows the second-order Raman modes including the LO+TA mode at 1115 cm^{-1}, 2TO mode at 1529 cm^{-1} and 2LO mode at 1716 cm^{-1} which are governed by optical phonons [56].

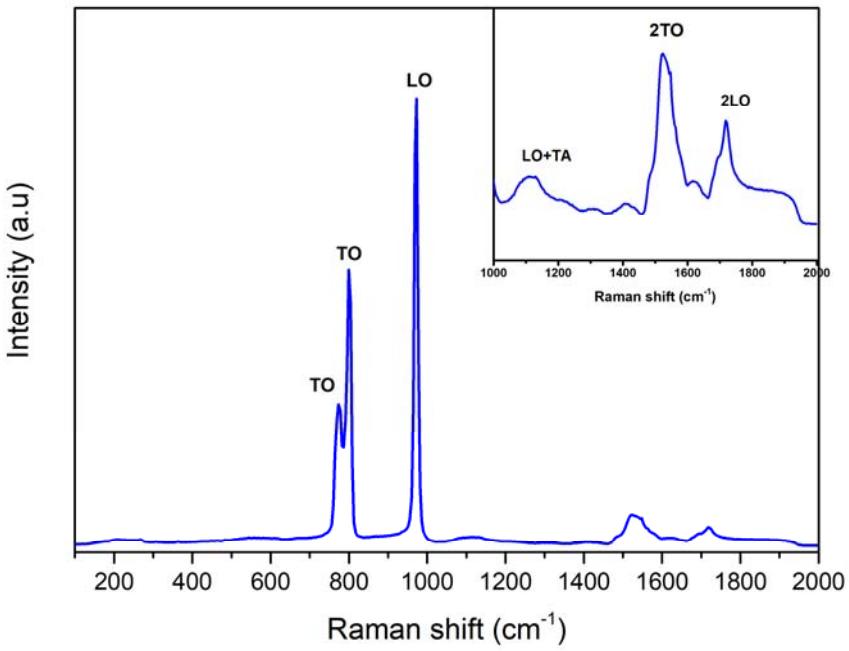

Fig. 3. *Raman spectrum of pristine polycrystalline SiC, the insert shows the magnified Raman spectrum in the region: 1000 – 2000 cm^{-1}.*

Fig. 4 (a) shows the as-implanted Raman spectra of Sr-SiC and Sr+He-SiC samples together with the Raman spectrum of the pristine sample for comparison. Fig. 4(b) shows the deconvoluted Raman spectra of Sr-SiC and Sr+He-SiC samples. The spectra show a breakdown of the Raman selection rules in the region 600-1000 cm^{-1} characterized by the obliteration of the SiC characteristic peaks, which is prominent in the co-implanted Sr+He-SiC. This is accompanied by the appearance of other bands caused by the destruction of the

chemical short-range resulting in the formation of the homonuclear bonds within the SiC network i.e., the Si-Si homonuclear bands between 0-600 cm^{-1}, and the C-C homonuclear bands between the regions 1100-1700 cm^{-1} [54, 57–59]. The two spectra have bands at 188 and 260 cm^{-1}, 192 and 253 cm^{-1}, for Sr-SiC and Sr+He-SiC, respectively, representing the crystalline Si (TA and LA+LO) [60–62]. The fitted bands at 510 and 514 cm^{-1} indicate to the amorphous Si in Sr-SiC and Sr+He-SiC, respectively [60–62]. The Sr-SiC spectrum displays first-order crystalline SiC bands at 781, 807, and 978 cm^{-1} Raman shifts [52,63], albeit less intense. The Sr+He-SiC spectrum exhibits amorphous bands in the Si-C region at 675, 775, 853, and 924 cm^{-1}[63, 64]. Both the Sr-SiC and Sr+He-SiC samples have a mixed amorphous sp^2/sp^3 C at 1423 and 1404 cm^{-1}, and similar observations have been observed in amorphous C [58, 59]. The resulting homonuclear bonds with crystalline and amorphous Si bands and C bands points to complete amorphization of the implanted SiC structures.

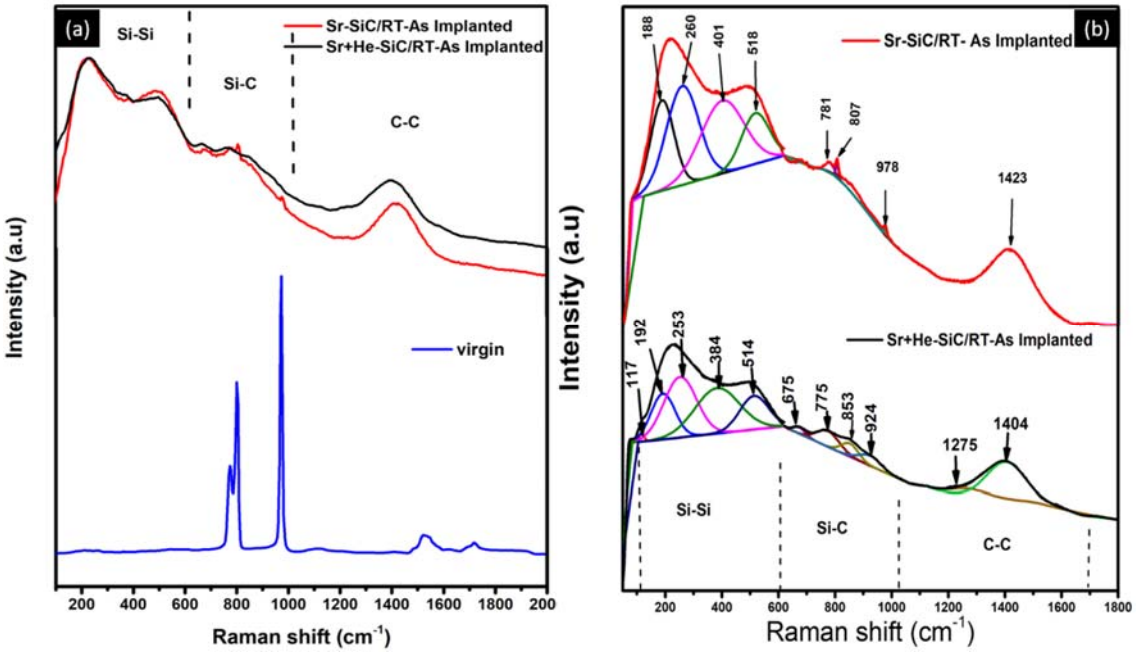

***Fig. 4**. (a) Sr-SiC (red) and Sr+He-SiC (black) as-implanted spectra with the virgin (blue) spectrum to compare. (b) Deconvoluted spectra of Sr-SiC (red) and Sr+He-SiC as-implanted spectra at RT.*

Fig. 5 (a) shows the Raman spectra of Sr-SiC samples isochronally annealed at temperatures from 1000 to 1300 ºC for 5 h, while Fig. 5 (b) shows the Raman spectra of Sr+He-SiC samples isochronally annealed in the same temperature range. Annealing at 1000 ºC of Sr-SiC sample resulted in a strong re-emergence of the SiC characteristic peaks between 600 and 1000 cm^{-1} with Si-Si homonuclear bands still present together with the C-C band splitting into D and G peaks. This re-emergence progressed with increasing temperature. However, a high

concentration of the Si-Si homonuclear bond network was still present in Sr -SiC samples annealed at temperatures below 1200 ºC. Raman characteristics peaks of SiC were fully restored in the samples annealed at 1200 and 1300 ºC indicating the recovery of most defects. Annealing of Sr+He-SiC sample at 1000 °C also caused some re-emergence of SiC with Si-Si homonuclear peak still present, this was accompanied by the appearance of the disordered diamond (D) and graphite (G) peaks and a shoulder in-between due to the mixed sp^2 and sp^3 coordination. Similarly, annealing at higher temperatures caused some re-emergence of SiC characteristic peaks with the Si-Si peak still present, accompanied by the appearance of the disordered diamond (D) and graphite (G) signals and a shoulder between them due to the mixed sp^2 and sp^3 coordination. The presence of Si-Si, D, and G in the samples annealed at higher temperatures indicates the poor healing of defects in the co-implanted samples, owing to the presence of He. In this study, the D and G peaks did not decompose at high temperatures, contrary to what was reported in ref. [65], where the peaks were found to decompose at temperatures above 500 ºC in 4H-SiC implanted with helium ions and then annealed from 300 to 1100 ºC. Hence, the implanted Sr plays a role in its stability.

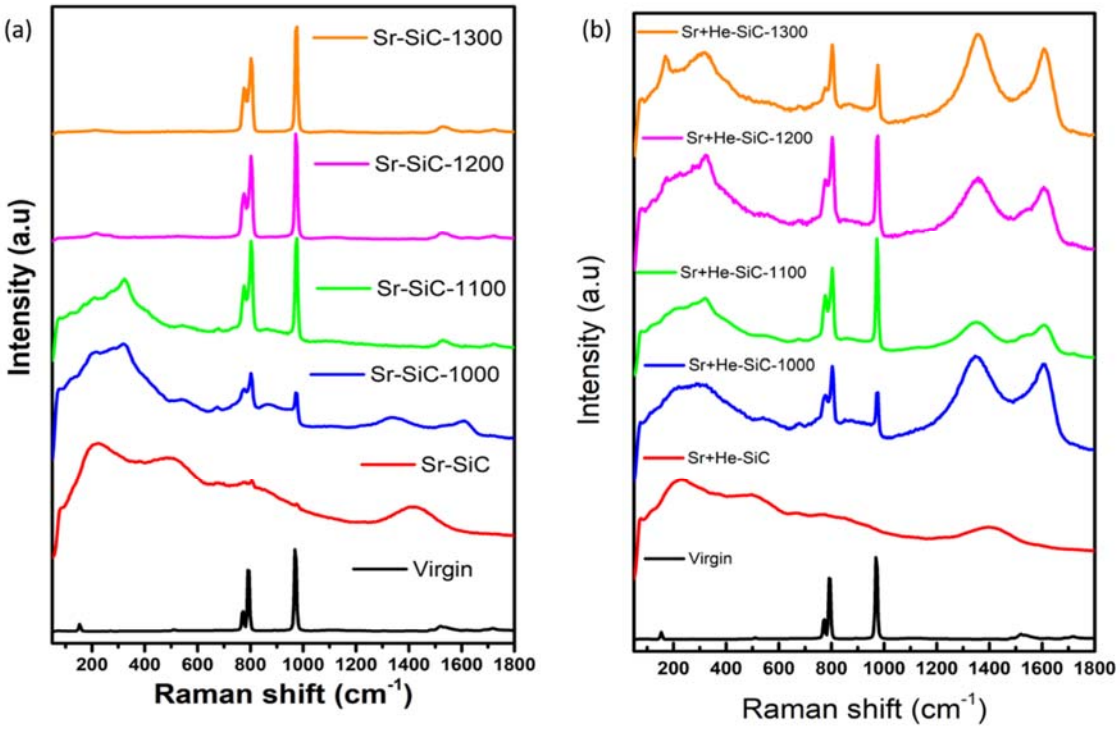

Fig. 5. *Average Raman spectra of (a) Sr-SiC, (b) Sr+He-SiC sequentially annealed at temperatures from 1000 to 1300 ºC for 5h, the pristine and as-implanted spectra are included for comparison.*

To better understand, the annealing of defects in the Sr-SiC and Sr+He-SiC samples, the relative Raman intensity (RRI) and Chemical disorder were calculated from the Raman spectra of Sr-SiC and Sr+He-SiC samples before and after annealing [65]. The RRI was calculated using equation 1 [66]:

$$RRI = \frac{I_{distorted}}{I_{crystalline}} \quad (1)$$

where $I_{distorted}$ is the average intensity of the treated SiC characteristic peaks and $I_{crystalline}$ is the average intensity of the pristine SiC characteristic peaks. The chemical disorder, χ, is defined in equation 2 as:

$$\chi = \frac{N_{C-C}}{N_{Si-C}} \approx \frac{I_{C-C}}{I_{Si-C}} \quad (2)$$

is the ratio of the concentration of C-C bonds ($N_{C\text{-}C}$) to that of heteronuclear bonds ($N_{Si\text{-}C}$) and it can be approximated in Raman spectra as the intensity of the C-C bonds ($I_{C\text{-}C}$) to Si-C bonds ($I_{Si\text{-}C}$). This is specified only for C atoms and is a close approximation of the homonuclear ratio R_{hnb}, defined for SiC as the ratio of the number of the homonuclear bonds to twice the number of heteronuclear bonds [66, 67]. Fig. 6 (a) shows the relative Raman intensity (RRI) of Sr-SiC and Sr+He-SiC samples as a function of annealing temperature. RRI is a measure of the number of defects in the material. RRI with a value of 1 indicates minimum defects in the material while a value of 0 indicates total disorder or amorphization. The RRI value of 0.05 and 0 were obtained for Sr-SiC and Sr+He-SiC samples, respectively, indicating total amorphization in the co-implanted SiC. This is also evident in Fig. 4 where Raman SiC characteristic peaks were not present in the Sr+He-SiC. Annealing of Sr-SiC caused progressive healing of defects with increasing annealing temperature and the full recrystallization was achieved after annealing at 1200 ºC: 30 % recovery at 1000 ºC, which increases to about 90 % at 1100 ºC and plateaus after 1200 ºC just below 100 %. In the Sr+He-SiC structure, the recovery was faster at 1000 ºC, just above 40 %. The structure reaches its highest recovery of 70 % at 1100 ºC, and the crystallinity was lost again at 1300 ºC. The difference in the healing of defects in the two samples is due to the presence of He. Nano-He bubbles already formed in the as-implanted Sr+He-SiC sample annealing might have caused the increased size of the bubbles or cavities which then increase the graphitization.

Fig. 6 (b) shows the chemical disorder of the Sr-SiC and Sr+He-SiC samples as a function of annealing temperature. The calculations were performed using the TO peak at 801 cm^{-1} for the

Si-C contribution and the peaks at 1423 and 1404 cm^{-1} for the C-C contribution in the Sr-SiC and Sr+He-SiC samples, respectively. The peak around 1500 cm^{-1} in the Sr-SiC annealed samples was used for the C-C contribution, while the peak between the D and G peak due to mixed sp^2 and sp^3 coordination was used in the Sr+He-SiC annealed sample. The ratio ranges from zero for perfect short-range order (SRO) and 1 for random short-range disorder. The Raman SiC characteristic peaks are completely obliterated in the as-implanted spectra. Therefore, single and co-implantation at room temperature resulted in $\chi = 1$, indicating maximum accumulation of chemical disorder and hence, total amorphization. The minimum chemical disorder needed for the formation of homonuclear bonds in SiC is at $\chi = 0.045$, while SRO cannot be maintained beyond the range $\chi = 0.39$-0.42 and a stable amorphous structure is achieved at $\chi \geq 0.54$ [68]. This confirms the observations of Fig. 5 and Fig. 6 (b), where the homonuclear bonds, specifically C-C bonds [Fig. 5 (a)] annihilated at 1100 ºC. However, at this temperature the Si-Si homonuclear bonds are still present despite the chemical disorder being less than 0.045. This is because the C-C bonds in the un-deformed system are stretched much larger than its equilibrium bond length and will break while the Si-Si and Si-C bonds are compressed [68]. The Sr+He-SiC samples after annealing at 1100 ºC retained some SRO with $\chi = 0.24$ just below the amorphization threshold. At 1200 ºC ($\chi = 0.35$) the structure is just at the threshold while at 1300 ºC ($\chi = 0.55$), the structure is heavily defected such that there are almost equal amounts of crystalline and amorphous regions.

The intensity ratio of the D peak and G peak, denoted as *ID/IG* was also calculated for as implanted and annealed samples Fig. 6 (c). The increase in this ratio indicates an increase in defects. Again, at 1100 ºC the number of defects in the C cluster decreases and the number of defects increases again at 1200 and 1300 ºC. Zandiatashbar et al. [69], have shown that ID/IG >1 indicates a structure marred with vacancy defects due to missing C atoms from their lattice sites. Hence, annealing the Sr+He-SiC sample at 1100 ºC caused a major restructuring allowing a limited recombination of C atoms with their vacancies, while the growing nano-bubbles and cavities further extends the vacancies as they push against the neighbouring atoms and forcing both Si and C atoms to agglomerate elsewhere. Hence, the presence of Si-Si homonuclear bands and graphite in Fig. 5 (b) after annealing. This agrees well with RRI and chemical disorder results.

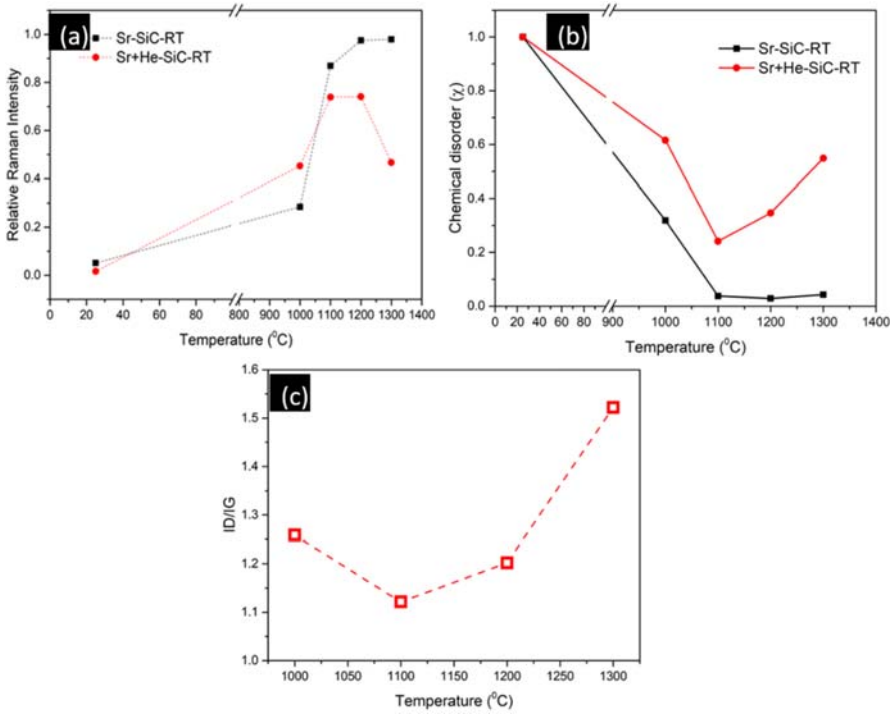

Fig. 6. *Relative Raman intensity (RRI) (a) Chemical disorder (b) for Sr and Sr+He implanted SiC and (c) the ratio of the D and G peak intensity of Sr+He-SiC, all with respect to annealing temperature.*

Fig. 7 shows the SEM micrographs of Sr-SiC before and after annealing. The SEM micrograph of the pristine SiC was discussed in ref [70]. The main feature of pristine SiC is the visibility of polishing marks on the surface. Implantation of Sr at RT resulted in the disappearance of polishing marks leaving a featureless structure. The disappearance of polishing marks in as-implanted SiC surface is due to swelling of the amorphous SiC [71], and/or sputtering induced by Sr implantation.. Annealing the Sr-SiC sample at 1000 °C resulted in some reappearance of polishing marks indicating some recrystallization after annealing. Annealing the Sr-SiC samples at temperatures between 1100 and 1300 ºC resulted in the formation of crystals on the surface. Consequently, the size and amount of the crystals increased with increasing annealing temperature, in line with the crystal growth theory [72].

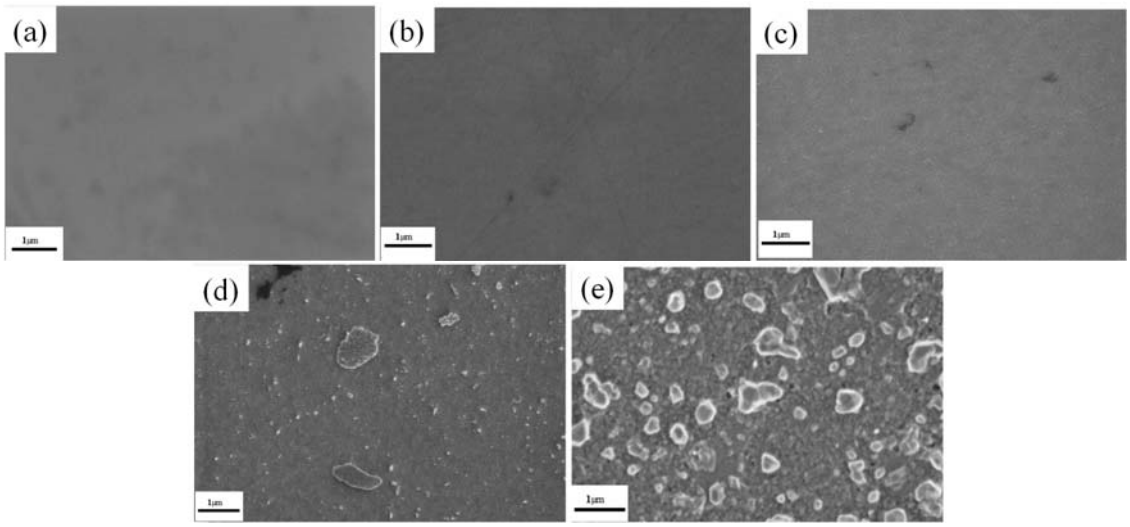

Fig. 7. *Surface SEM micrographs of (a) as implanted Sr-SiC and as-implanted Sr-SiC samples annealed at (b) 1000 °C; (c) 1100 °C; (d) 1200 °C, and (e) 1300 °C for 5 hours.*

Fig. 8 shows the SEM micrographs of the Sr+He-SiC samples before and after isochronal annealing. Similar to the as-implanted micrograph of Sr-SiC, the micrograph of Sr+He-SiC has a featureless surface indicating amorphization. Hence, the effect of nano-bubbles in Sr+He-SiC as observed from TEM results has no observable effect on the surface. Annealing at 1000 ºC resulted in the appearance of cornflower-like structures on the surface accompanied by the appearance of polishing marks. Without a doubt, the appearance of polishing marks indicates some recrystallization, while the appearance of cornflower-like structures is due to the presence of He. Annealing at 1100 °C caused an increase in the size of the cornflower structures. This was further accompanied by the appearance of crystallites and pores. The appearance of crystallites indicates further recrystallization at this temperature. Further annealing at higher temperatures up to 1300 °C caused the number and size of the cornflower structures to increase significantly. Bigger crystallites start to form around the bigger cornflower structure edges after annealing from 1200 ºC. These crystallites increase in size after annealing at 1300 °C and form what looks like nano-sunflower petals around the cornflowers.

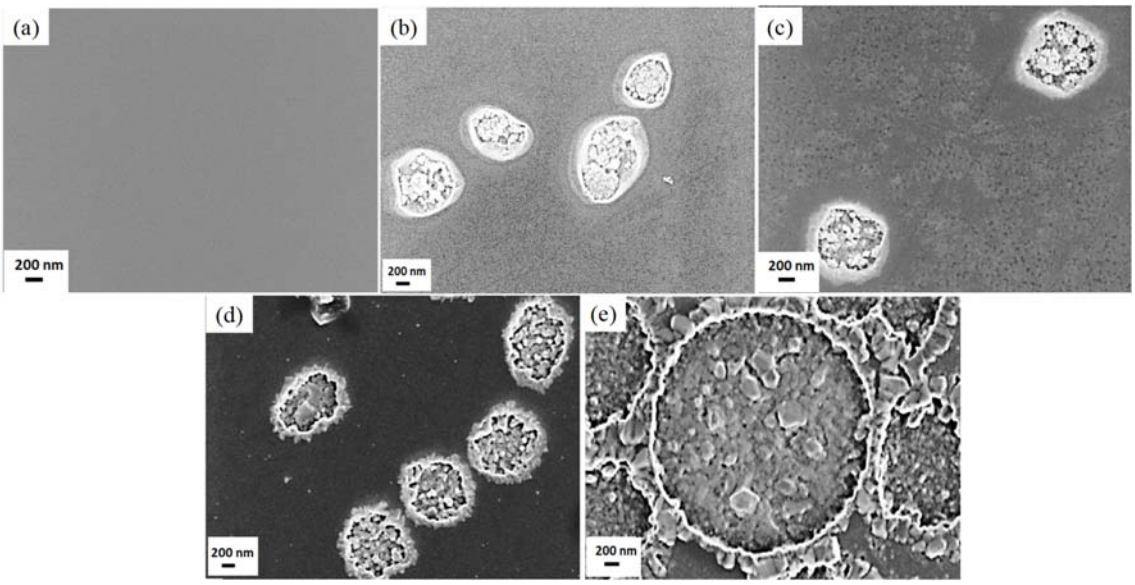

***Fig. 8**. SEM micrographs of Sr+He-SiC (a) before and after isochronnally annealed at (b) 1000 °C; (c) 1100 °C; (d) 1200 °C, and (e) 1300 °C for 5 hours.*

The cornflowers formed in the annealed Sr+He-SiC samples are due to the presence of He as they were not observed in Sr-SiC annealed at the same temperatures. As it has been seen in the TEM results in Fig. 2, the as-implanted Sr+He-SiC sample already has nano-He bubbles. Hence the cornflowers might be due to agglomeration of He nanobubbles assisted by defects and temperature resulting in blisters on the surfaces and their subsequent rapture or to the exfoliation of the surface layer due to the high helium pressure within the bubbles below the surface resulting in the formation of holes. Distinguishing between blisters and holes in SEM micrographs is challenging. Therefore, the as-implanted and annealed Sr+He-SiC samples were further characterized by AFM.

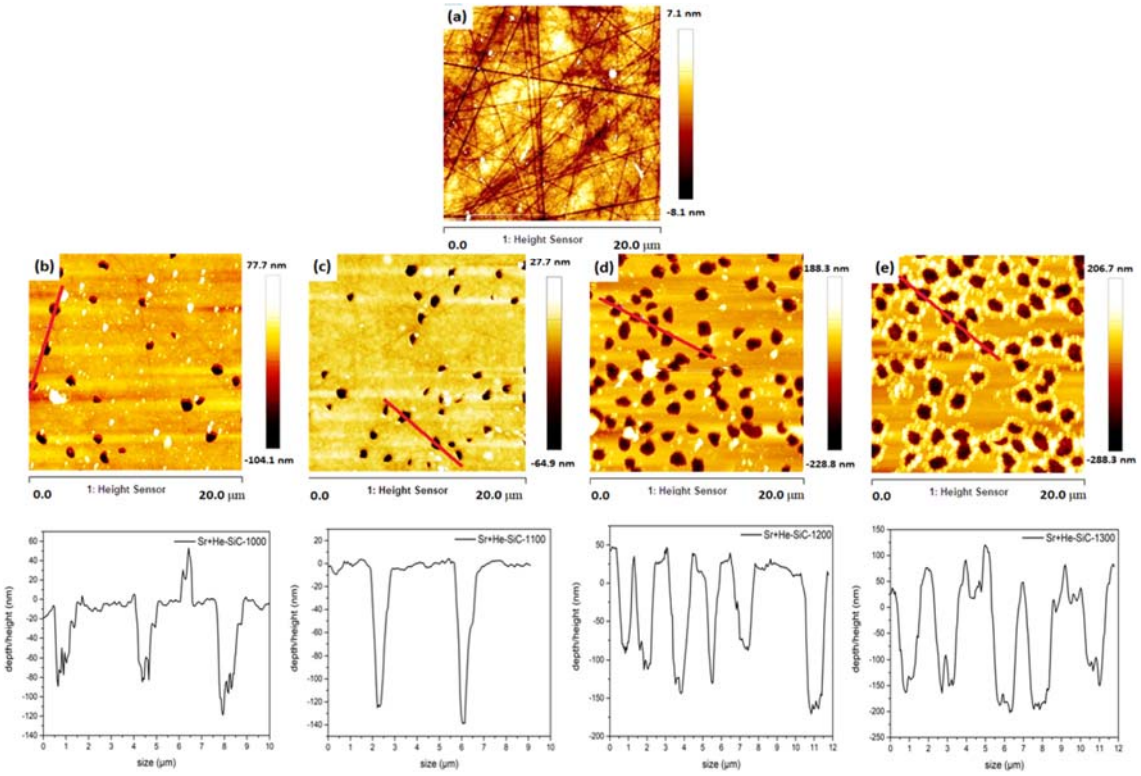

Fig. 9. *AFM micrograms of as-implanted Sr+He-SiC before annealing (a), and after isochronal annealing at 1000 ºC, (b) 1100 ºC (c), 1200 ºC (d) and 1300 ºC (e) for 5 hours. Their corresponding profiles of lines marked profiles are also shown. The white particles are dust partiles.*

Fig. 9 shows AFM micrographs of Sr+He-SiC samples before and after annealing together with the depth profiles of the line marked in the micrographs. Fig. 9 (a) shows no blisters or exfoliation on the surface of the as-implanted Sr+He-SiC in agreement with SEM results. After annealing at 1000 ºC, the surface exfoliated resulting in the appearance of holes on the surface. This is due to the high internal pressure within the He bubbles as they grow and agglomerate underneath the surface. These holes are of different shapes and size and appear as a dark colour, indicative of the depth according to the scale bar of the height. The number and size of the holes increase with increasing annealing temperature, thus agreeing with SEM. The bigger the holes, the more they swallow the smaller holes and become even bigger, resulting in an accumulative growth of the holes. After annealing at 1200 ºC in Fig. 9 (d), crystallites as discussed in SEM, are observed and here too, increase in size with increasing temperature and appear as around holes (or cornflower morphology). The hole depths also increase with temperature and vary from about 100 nm at 1000 ºC to about 200 nm at 1300 ºC.

The cornflowers observed in SEM for the Sr+He-SiC annealed samples are confirmed by AFM as holes. After annealing, microstructural reordering leads to the formation and agglomeration of surface-parallel nanobubbles below the surface, producing bigger He bubbles. Given the right conditions; size and internal gas pressure within the bigger He-bubbles, the surface blisters will emerge providing stress relief below the surface. When the blisters reach a critical diameter (d_c) and sufficient height (h) from the surface such that $h/d_c << 1$, and when the critical pressure exerted by He on the blister wall, and the stress intensity factor at the crack tip, K_I, is higher than the fracture toughness of the material, they erupt/fracture leaving holes behind [73, 74, 75]. The formation of these holes also depends on the minimum number of nanobubbles needed to initiate the rupture, and the elastic deformation of the blisters' highest point. Annealing of Sr+He-SiC did not form blisters on the surface but rather only holes. This suggests that when annealing from 1000 ºC for 5 h, the microstructural rearrangements cause an interaction of the bigger bubbles with the implanted Sr. This creates stress around the bigger bubbles such that the blisters do not get a chance to form on the surface. As the temperature increases, the number of nanobubbles coalescing increases too, leading to the increase in the number of holes. The bigger holes combine with the neighbouring smaller ones creating even larger holes (or accumulative growth of holes) as seen in Fig. 9 (b-e).

Fig. 10 shows the Sr and He ERDA depth profiles of the Sr-SiC and Sr+He-SiC samples before and after annealing at 1000 ºC. The Sr profile of the as-implanted in Sr-SiC, Fig. 10 (a), agrees reasonably well with the SRIM simulation and RBS Sr profile previously studied [76]. Annealing the Sr-SiC at 1000 ºC resulted in a slight migration of Sr towards the surface. The as-implanted Sr profile in the Sr+He-SiC sample has shifted towards the surface as compared to the as-implanted profile of Sr-SiC sample. The range also changed from 250 nm to 200 nm in the as-implanted Sr+He-SiC. This is due to the displacement of Sr atoms by the formation of He-nanobubbles close to the end of range of Sr. Annealing the Sr+He-SiC sample at 1000 ºC resulted in the migration of Sr towards the surface accompanied by some loss of Sr from the surface. This caused the Sr profile to have double peaks with a minimum around 120 nm, suggesting trapping as indicated in Fig. 10 (b). Similar behaviour of Fe atoms was noticed in Fe+He implanted SiC after annealing [39]. An almost complete loss of implanted He due to out-diffusion was also observed after annealing at 1000 ºC in Fig. 10 (c). Out diffusion of He leaves cavities in the implanted region, which might be responsible for the trapping of Sr.

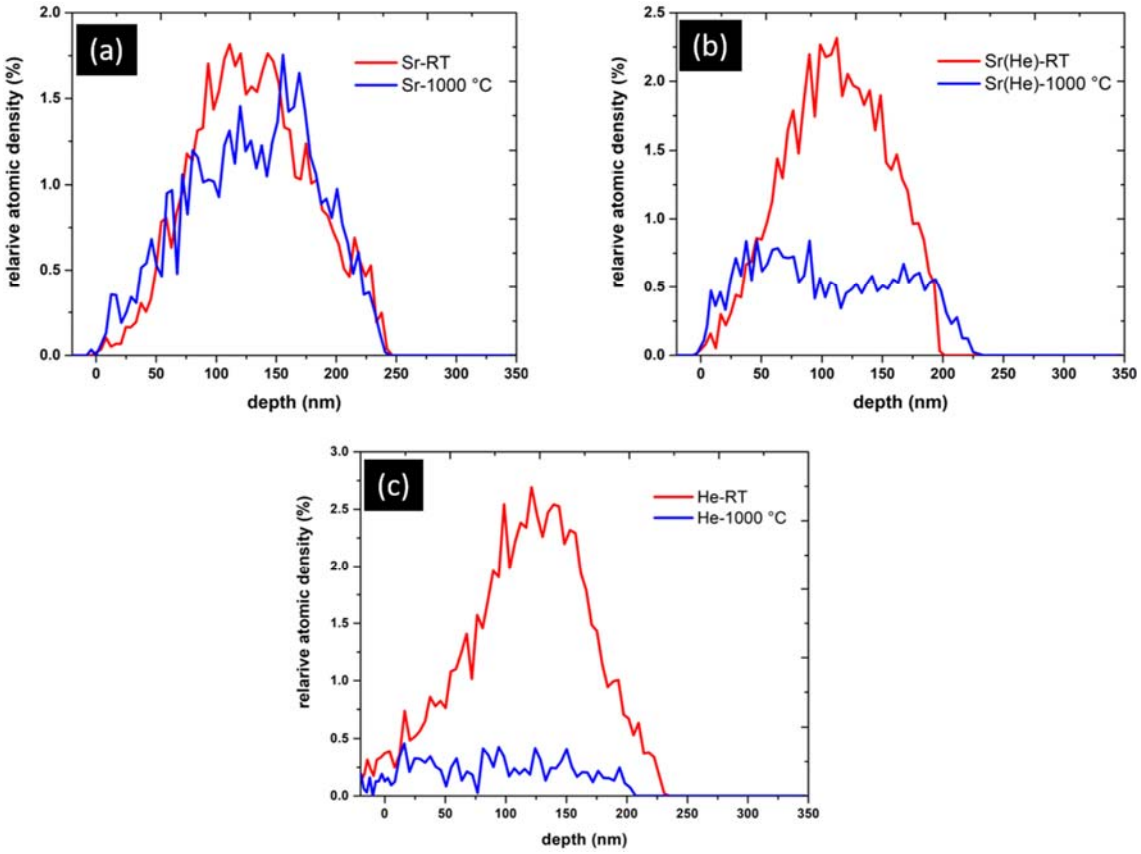

Fig. 10. *ERDA depth profiles of as-implanted and annealed (a) Sr in the Sr-SiC sample, (b) Sr in Sr+He-SiC sample, and (c) He in Sr+He-SiC sample.*

Fig. 11 shows the bright field TEM micrographs Sr+He-SiC sample annealed at 1000 ºC for 5 h together with the high magnification of the implanted region. The arrows in the micrographs have the same meaning as in Fig. 2. Annealing the Sr+He-SiC sample at 1000 ºC caused the reduction of the damage layer thickness from about 300 nm to about 287 nm due to epitaxial recrystallization from the amorphous-crystalline (a-c) interface. Some recrystallization was observed in the damage layer as indicated by the appearance of crystalline structures or fringes in the damage region of the annealed TEM micrograph. Moreover, He cavities (appearing white in Fig. 11) with most forming cavity network are observed in the damage region of the annealed sample. Some darker regions are also observed in the TEM micrograph of the annealed sample. The almost complete out-diffusion of He in the sample annealed at 1000 ºC (Fig. 10 (c)) together with the appearance of brighter regions in the TEM micrograph confirm that the brighter regions are cavities not He bubbles, while the darker regions might be cavities with Sr. The minimum of the Sr profile (Fig.10) of the annealed sample is around 120 nm which corresponds with the region with cavity network in the TEM micrograph and the two peaks

correspond with the darker regions/darker cavities in the micrograph. Hence, Sr is trapped in the cavities.

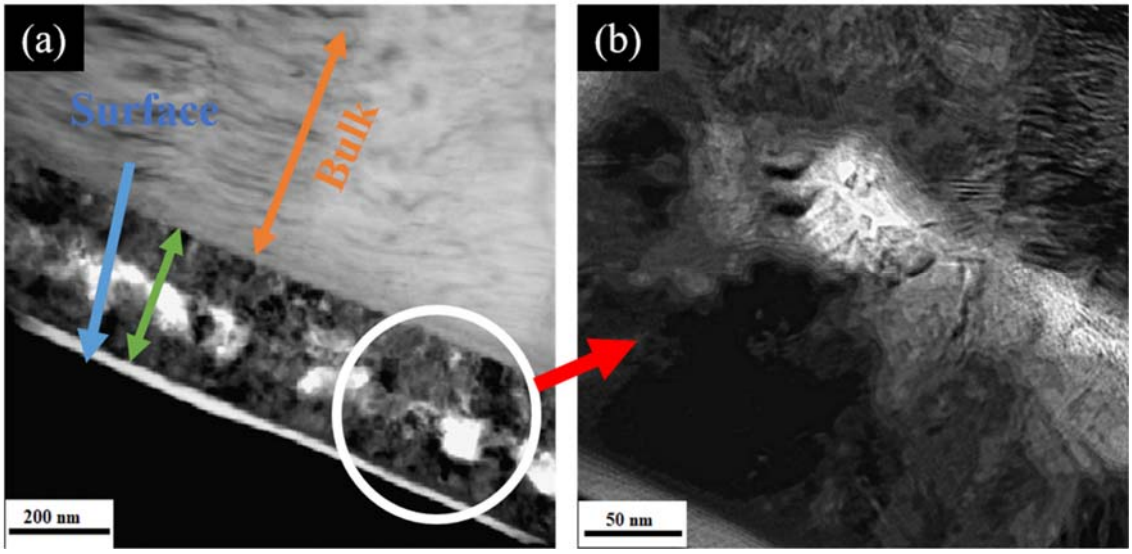

Fig. 11. *Bright field (BF) TEM micrographs of Sr & He implanted SiC annealed at 1000 ºC. (b) Detailed bubbles in the implanted layer at higher magnification.*

Accumulation of chemical disorder drives the crystalline-to-amorphization (c-a) transition, and this is characterized by the formation of homonuclear bonds. The formation of homonuclear bonds is a result of antisite formation. Therefore, the higher the chemical disorder in the material, the higher the number of antisite defects, hence, the formation of the D and G peaks in the Sr+He-SiC annealed samples. The formation of the D and G peaks in the annealed Sr+He-SiC samples with no formation of D and G peaks in the annealed Sr-SiC samples is no doubt an indication that He is a driving force in their formation. When He atoms are implanted into SiC, some of them are trapped by C and Si [25, 77, 78] interstitials, while others are trapped by vacancies, dislocation loops and complex defects. Those trapped by Si interstitials will have strong interactions with nearby carbons [73] and these C atoms will accumulate around the He atoms. The migration energy of C and Si interstitials is 0.74 and 1.53 eV, respectively [79], while the migration energy of C and Si vacancies is 3.2-3.6 eV and 3.5-5.2 eV, respectively [80]. Thus, the mobility of vacancies is only possible at temperatures above 1260 ºC in SiC [81]. Therefore, below 1260 ºC annealing temperatures, the vacancies with trapped helium atoms will not be able to move, thus the formation of bubbles will be from the movement of interstitially trapped helium atoms. These bubbles will be the nuclei of graphitic formation. Most of the interstitially trapped helium would have coalesced and released at 1000 ºC. Then the relaxation and recovery processes will take place at 1100 ºC since no He-trapped vacancies

will be moving to facilitate He agglomeration. This explains why no increase in the size or number of holes were observed in AFM at 1100 ºC and why the maximum crystallinity and short-range order occurred at the same temperature. Since the vacancy trapped helium atoms have enough energy to move above 1260 ºC, in our case, given the 5 h duration of annealing, we have reason to believe the movement of these vacancies happens at 1200 ºC. This movement of vacancies and coalescence of helium atoms further enables the formation of antisites and therefore, the increase in concentration of homonuclear bonds and as a consequence, graphitic formation. As discussed above, the bubbles do not get the chance to form blisters on the surface, they emerge from the surface already with a special combination of diameters above the needed critical diameter, i.e., above minimum number of nanobubbles needed to erupt/fracture and the necessary stress from the movement of Sr implants. Also, an increase in chemical disorder leads to the emergence of holes on the surface of SiC [68]. The emergence of nanocavities leads to a decrease in surface strength at $\chi > 0.045$ [68]. This decrease in strength makes it hard for the surface to contain high-pressure helium bubbles and hence, no blisters on the surface. The ERDA results show that after annealing there is a segregation of Sr implants around the depth of the cavities proving that the cavities are trap-zones for Sr implants. This was also confirmed by TEM.

3. Summary

In this study, the role of He in the structural modification of polycrystalline SiC pre-implanted with Sr ions and on the migration of Sr was investigated. Sr was first implanted into SiC at RT and followed by helium ions also at RT. The implanted Sr+He-SiC samples were then isochronally annealed from 1000 to 1300 ºC for 5 h. The results were compared with those of Sr implanted SiC (Sr-SiC) samples isochronally annealed at the same temperatures. Co-implantation of helium at RT resulted in the formation of helium nanobubbles band around the projected range of the implants, which resulted in an increase in the damage layer from 304 nm in the Sr-SiC to about 311 nm in the Sr+He-SiC. Cornflower-like structures were formed on the surface of Sr+He-SiC annealed samples and increased with temperature. These were as a result of exfoliation of the surface and escape of helium gas. Graphitization of the structure was due to homonuclear bond formation as a result of antisite defects and the ability of C-C to reorganise at high temperatures. Helium cavities below the surface form at a depth around the projected range of Sr and He. Sr was observed to segregate after annealing around the cavities. No blisters were observed, and almost all helium out-diffused after 1000 ºC. These are

important observations and can offer insights in the use of SiC in both fusion and fission reactors.

Declaration of Competing Interest

The authors declare that they have no known competing financial interests or personal relationships that could have appeared to influence the work reported in this paper.

Acknowledgements

This study was financially supported by the National Research Foundation (NRF) of South Africa (grant numbers 120471 and 120804) which is gratefully acknowledged.

4. References

[1] J.N. Shenoy, J.A Cooper, M.R. Melloch, High-voltage double-implanted power MOSFET's in 6H-SiC. IEEE Electron Device Lett., 18(3) (1997) 93-95, https://doi.org/10.1109/55.556091

[2] Q. Jia, K. Huang, T. You, A. Yi, J. Lin, S. Zhang, M. Zhou, B. Zhang, B. Zhang, W. Yu, X. Ou, Freestanding ultrathin single-crystalline SiC substrate by MeV H ion-slicing. Appl. Phys. Lett., 112(19) (2018) 192102, https://doi.org/10.1063/1.5025889

[3] S. Castelletto, B.C. Johnson, V. Ivády, N. Stavrias, T. Umeda, A. Gali, T. Ohshima, A silicon carbide room-temperature single-photon source. Nature materials, 13(2) (2014) 151-156, https://doi.org/10.1038/nmat3806

[4] A. Yi, Y. Zheng, H. Huang, J. Lin, Y. Yan, T. You, K. Huang, S. Zhang, C. Shen, M. Zhou, W. Huang, Wafer-scale 4H-silicon carbide-on-insulator (4H–SiCOI) platform for nonlinear integrated optical devices. Opt. Mater., 107 (2020) 109990, https://doi.org/10.1016/j.optmat.2020.109990

[5] J. Cardenas, M. Yu, Y. Okawachi, C.B. Poitras, R.K. Lau, A. Dutt, A.L. Gaeta, M. Lipson, Optical nonlinearities in high-confinement silicon carbide waveguides. Opt. Lett., 40(17) (2015) 4138-4141, https://doi.org/10.1364/OL.40.004138

[6] D. Guo, H. Zang, P. Zhang, J. Xi, T. Li, L. Ma, C. He, Analysis of primary damage in silicon carbide under fusion and fission neutron spectra. Journal of Nuclear Materials, 455(1-3) (2014) 229-233, https://doi.org/10.1016/j.jnucmat.2014.06.001

[7] Y. Katoh, K. Ozawa, C. Shih, T. Nozawa, R.J. Shinavski, A. Hasegawa, L.L. Snead, Continuous SiC fiber, CVI SiC matrix composites for nuclear applications: Properties and irradiation effects. J. Nucl. Mater., 448(1-3) (2014) 448-476, https://doi.org/10.1016/j.jnucmat.2013.06.040

[8] C.H. Carter Jr, R.F. Davis, J. Bentley, Kinetics and mechanisms of high-temperature creep in silicon carbide: II, chemically vapor deposited. J. Am. Ceram. Soc., 67(11) (1984) 732-740, https://doi.org/10.1111/j.1151-2916.1984.tb19510.x

[9] V.A. Avincola, M. Grosse, U. Stegmaier, M. Steinbrueck, H.J. Seifert, Oxidation at high temperatures in steam atmosphere and quench of silicon carbide composites for nuclear application. Nucl. Eng. Des., 295 (2015) 468-478, https://doi.org/10.1016/j.nucengdes.2015.10.002

[10] B.A. Pint, K.A. Terrani, M.P. Brady, T. Cheng, J.R. Keiser, High temperature oxidation of fuel cladding candidate materials in steam–hydrogen environments. J. Nucl. Mater., 440(1-3) (2013) 420-427, https://doi.org/10.1016/j.jnucmat.2013.05.047

[11] L.L. Snead, T. Nozawa, M. Ferraris, Y. Katoh, R. Shinavski, M. Sawan, Silicon carbide composites as fusion power reactor structural materials. J. Nucl. Mater., 417(1-3) (2011) 330-339, https://doi.org/10.1016/j.jnucmat.2011.03.005

[12] L.L. Snead, T. Nozawa, Y. Katoh, T.S. Byun, S. Kondo, D.A. Petti, Handbook of SiC properties for fuel performance modeling. J. Nucl. Mater., 371(1-3) (2007) 329-377, https://doi.org/10.1016/j.jnucmat.2007.05.016

[13] Y. Katoh, A. Kohyama, T. Nozawa, M. Sato, SiC/SiC composites through transient eutectic-phase route for fusion applications. J. Nucl. Mater., 329 (2004) 587-591, https://doi.org/10.1016/j.jnucmat.2004.04.157

[14] Y. Katoh, L.L. Snead, C.H. Henager Jr, A. Hasegawa, A. Kohyama, B. Riccardi, H. Hegeman, Current status and critical issues for development of SiC composites for fusion applications. J. Nucl. Mater., 367 (2007) 659-671, https://doi.org/10.1016/j.jnucmat.2007.03.032

[15] N.M. George, K. Terrani, J. Powers, A. Worrall, I. Maldonado, Neutronic analysis of candidate accident-tolerant cladding concepts in pressurized water reactors. Ann. Nucl. Energy, 75 (2015) 703-712, https://doi.org/10.1016/j.anucene.2014.09.005

[16] G.J. Butterworth, Low activation structural materials for fusion. Fusion Eng. Des., 11(1-2) (1989) 231-244, https://doi.org/10.1016/0920-3796(89)90021-5

[17] K.A. Terrani, B.A. Pint, C.M. Parish, C.M. Silva, L.L. Snead, Y. Katoh, Silicon carbide oxidation in steam up to 2 MPa. J. Am. Ceram. Soc., 97(8) (2014) 2331-2352, https://doi.org/10.1111/jace.13094

[18] M.R. Gilbert, J.C. Sublet, Neutron-induced transmutation effects in W and W-alloys in a fusion environment. Nucl. Fusion, 51(4) (2011) 043005, https://doi.org/10.1088/0029-5515/51/4/043005

[19] A. Barcz, M. Kozubal, R. Jakieła, J. Ratajczak, J. Dyczewski, K. Gołaszewska, T. Wojciechowski, G.K. Celler, Diffusion and impurity segregation in hydrogen-implanted silicon carbide. J. Appl. Phys., 115(22) (2014) 223710, https://doi.org/10.1063/1.4882996

[20] J. Grisolia, F. Cristiano, B. De Mauduit, G.B. Assayag, F. Letertre, B. Aspar, L. Di Cioccio, A. Claverie, Kinetic aspects of the growth of hydrogen induced platelets in SiC. J. Appl. Phys., 87(12) (2000) 8415-8419, https://doi.org/10.1063/1.373556

[21] C.H. Chen, Y. Zhang, Y. Wang, M.L. Crespillo, C.L. Fontana, J.T. Graham, G. Duscher, S.C. Shannon, W.J. Weber, Dose dependence of helium bubble formation in nano-engineered SiC at 700° C. J. Nucl. Mater., 472 (2016) 153-160, https://doi.org/10.1016/j.jnucmat.2016.01.029

[22] J.A. Hinks, J.A. Van Den Berg, S.E. Donnelly, MIAMI: Microscope and ion accelerator for materials investigations. J. Vac. Sci. Technol. A: Vac. Surf. Films, 29(2) (2011) 021003, https://doi.org/10.1116/1.3543707

[23] B.S. Li, Y.Y. Du, Z.G. Wang, Recrystallization of He-ion implanted 6H-SiC upon annealing. Nucl. Instrum. Methods Phys. Res B., 345 (2015) 53-57, https://doi.org/10.1016/j.nimb.2014.12.049

[24] B.S. Li, Z.G. Wang, C.H. Zhang, K.F. Wei, C.F. Yao, J.R. Sun, M.H. Cui, Y.F. Li, H.P. Zhu, Y.Y. Du, Y.B. Zhu, Evolution of strain and mechanical properties upon annealing in He-implanted 6H-SiC. J. Nucl. Mater., 455(1-3) (2014) 116-121, https://doi.org/10.1016/j.jnucmat.2014.05.028

[25] F. Linez, F. Garrido, H. Erramli, T. Sauvage, B. Courtois, P. Desgardin, M.F. Barthe, Experimental location of helium atoms in 6H–SiC crystal lattice after implantation and after annealing at 400° C. J. Nucl. Mater., 459 (2015) 62-69, https://doi.org/10.1016/j.jnucmat.2014.12.118

[26] F. Linez, E. Gilabert, A. Debelle, P. Desgardin, M.F. Barthe, Helium interaction with vacancy-type defects created in silicon carbide single crystal. J. Nucl. Mater., 436(1-3) (2013) 150-157, https://doi.org/10.1016/j.jnucmat.2013.01.288

[27] C.H. Zhang, S.E. Donnelly, V.M. Vishnyakov, J.H. Evans, Dose dependence of formation of nanoscale cavities in helium-implanted 4H–SiC. J. Appl. Phys., 94(9) (2003) 6017-6022, https://doi.org/10.1063/1.1611630

[28] J. Sun, B.S. Li, Y.W. You, J. Hou, Y. Xu, C.S. Liu, Q.F. Fang, Z.G. Wang, The stability of vacancy clusters and their effect on helium behaviors in 3C-SiC. J. Nucl. Mater., 503 (2018) 271-278, https://doi.org/10.1016/j.jnucmat.2018.03.010

[29] N. Daghbouj, B.S. Li, M. Callisti, H.S. Sen, J. Lin, X. Ou, M. Karlik, and T. Polcar. The structural evolution of light-ion implanted 6H-SiC single crystal: Comparison of the effect of helium and hydrogen. Acta Mater., 188 (2020), pp.609-622, https://doi.org/10.1016/j.actamat.2020.02.046

[30] N. Daghbouj, B.S. Li, M. Callisti, H.S. Sen, M. Karlik, and T.J.A.M. Polcar. Microstructural evolution of helium-irradiated 6H–SiC subjected to different irradiation conditions and annealing temperatures: A multiple characterization study. Acta Mater., 181 (2019), pp.160-172, https://doi.org/10.1016/j.actamat.2019.09.027

[31] W. Han, B. Li, B., Microstructural defects in He-irradiated polycrystalline α-SiC at 1000° C. J. Nucl. Mater., 504 (2018) 161-165, https://doi.org/10.1016/j.jnucmat.2018.03.038

[32] B.S. Li, Y.Y. Du, Z.G. Wang, K.F. Wei, H.P. Zhang, C.F. Yao, H.L. Chang, J.R. Sun, M.H. Cui, Y.B. Sheng, L.L. Pang, Transmission electron microscopy investigations of bubble formation in He-implanted polycrystalline SiC. Vac., 113 (2015) 75-83, https://doi.org/10.1016/j.vacuum.2014.12.017

[33] M. Liu, X. Yang, Y. Gao, R. Liu, H. Huang, X. Zhou, T.K. Sham, Investigation of the damage behavior in CVD SiC irradiated with 70 keV He ions by NEXAFS, Raman and TEM. J. Eur. Ceram. Soc., 37(4) (2017) 1253-1259, https://doi.org/10.1016/j.jeurceramsoc.2016.11.046

[34] E. Oliviero, M.L. David, M.F. Beaufort, J. Nomgaudyte, L. Pranevicius, A.B.J.F. Declemy, J.F. Barbot, Formation of bubbles by high dose He implantation in 4H–SiC. J. Appl. Phys., 91(3) (2002) 1179-1186, https://doi.org/10.1063/1.1429760

[35] S. Gavarini, J. Baillet, N. Millard-Pinard, V. Garnier, C. Peaucelle, X. Jaurand, C. Bernard, R. Rapegno, S. Cardinal, C. Dalverny, B. Lanfant, Effects of helium irradiation on fine grained β-SiC synthesized by spark plasma sintering. J. Eur. Ceram. Soc., 40(1) (2020) 1-11, https://doi.org/10.1016/j.jeurceramsoc.2019.09.018

[36] B. Li, C. Zhang, H. Liu, L. Xu, X. Wang, Z. Yang, F. Ge, W. Gao, T. Shen, T., Microstructural and elemental evolution of polycrystalline α-SiC irradiated with ultra-

high-fluence helium ions before and after annealing. Fusion Eng. Des., 154 (2020) 111511, https://doi.org/10.1016/j.fusengdes.2020.111511

[37] H. Zang, W. Jiang, W. Liu, A. Devaraj, D.J. Edwards, C.H. Henager Jr, R.J. Kurtz, T. Li, C. He, D. Yun, Z. Wang, Vacancy effects on the formation of He and Kr cavities in 3C-SiC irradiated and annealed at elevated temperatures. Nucl. Instrum. Methods Phys. Res B., 389 (2016) 40-47, https://doi.org/10.1016/j.nimb.2016.11.017

[38] T.T. Hlatshwayo, C.E. Maepa, M. Msimanga, M. Mlambo, E.G. Njoroge, V.A. Skuratov, S.V. Motloung, J.B. Malherbe, Helium assisted migration of silver implanted into SiC. Vac., 183 (2021) 109865, https://doi.org/10.1016/j.vacuum.2020.109865

[39] B.S. Li, H.S. Sen, N. Daghbouj, A.T. AlMotasem, J. Lorinčík, M. Karlik, F.F. Ge, L. Zhang, Z. Sofer, I. Elantyev, and M. Callisti. Thermal behavior of iron in 6H-SiC: Influence of He-induced defects. Scr. Mater., 218 (2022), p.114805, https://doi.org/10.1016/j.scriptamat.2022.114805

[40] G. You, S. Wang, H. Zhang, W. Li, X. Guo, S. Ru, and B. Li.. Chemical Disorder in 6H-SiC Irradiated with Both He and Fe Ions Followed by 1500° C Annealing: Electron Energy-Loss Spectroscopy Analysis. Crystals, 12(5) (2022), p.687, https://doi.org/10.3390/cryst12050687

[41] S.S. Dwaraknath, G.S. Was, G.S., Radiation enhanced diffusion of cesium, strontium, and europium in silicon carbide. J. Nucl. Mater., 474 (2016) 76-87, https://doi.org/10.1016/j.jnucmat.2016.02.034

[42] T.T. Hlatshwayo, N. Mtshonisi, E.G. Njoroge, M. Mlambo, M. Msimanga, V.A. Skuratov, J.B. Malherbe, S.V. Motloung, Effects of Ag and Sr dual ions implanted into SiC. Nucl. Instrum. Methods Phys. Res B., 472 (2020) 7-13, https://doi.org/10.1016/j.nimb.2020.03.035

[43] E. Friedland, J.B. Malherbe, N.G. Van der Berg, T. Hlatshwayo, A.J. Botha, E. Wendler, W. Wesch, Study of silver diffusion in silicon carbide. J. Nucl. Mater., 389(2) (2009) 326-331, https://doi.org/10.1016/j.jnucmat.2009.02.022

[44] S.S. Dwaraknath, G.S. Was, G.S., The diffusion of cesium, strontium, and europium in silicon carbide. Journal of Nuclear Materials, 476 (2016) 155-167, https://doi.org/10.1016/j.jnucmat.2016.04.034

[45] M. Msimanga, D. Wamwangi, C.M. Comrie, C.A. Pineda-Vargas, M. Nkosi, T. Hlatshwayo, The new Heavy Ion ERDA set up at iThemba LABS Gauteng: Multilayer thin film depth profiling using direct calculation and Monte Carlo simulation codes. Nucl. Instrum. Methods Phys. Res B., 296 (2013) 54-60,

https://doi.org/10.1016/j.nimb.2012.11.015

[46] K. Arstila, J. Julin, M.I. Laitinen, J. Aalto, T. Konu, S. Kärkkäinen, S. Rahkonen, M. Raunio, J. Itkonen, J.P. Santanen, T. Tuovinen, Potku–New analysis software for heavy ion elastic recoil detection analysis. Nucl. Instrum. Methods Phys. Res B., 331 (2014) 34-41, https://doi.org/10.1016/j.nimb.2014.02.016

[47] J.F. Ziegler, M.D. Ziegler, J.P. Biersack, SRIM–The stopping and range of ions in matter (2010). Nucl. Instrum. Methods Phys. Res B., 268(11-12) (2010) 1818-1823, https://doi.org/10.1016/j.nimb.2010.02.091

[48] W.J. Weber, L.M. Wang, N. Yu, The irradiation-induced crystalline-to-amorphous phase transition in α-SiC. Nucl. Instrum. Methods Phys. Res B., 116(1-4) (1996) 322-326, https://doi.org/10.1016/0168-583X(96)00066-3

[49] J. Li, H. Huang, G. Lei, Q. Huang, R. Liu, D. Li, and L. Yan. Evolution of amorphization and nanohardness in SiC under Xe ion irradiation. J. of Nucl. Mater., 454(1-3) (2014), pp.173-177, https://doi.org/10.1016/j.jnucmat.2014.07.036

[50] T. Zhang, X, He, L. Chen, J. Li, Q. Liao, S. Xu, P. Zheng, B. Li, The effect of cavities on recrystallization growth of high-fluence He implanted-SiC. Nucl. Instrum. Methods Phys. Res B., 509 (2021) 68-72, https://doi.org/10.1016/j.nimb.2021.08.012

[51] S.G. Sridhara, T.J. Eperjesi, R.P. Devaty, W.J. Choyke, Penetration depths in the ultraviolet for 4H, 6H and 3C silicon carbide at seven common laser pumping wavelengths. Mater. Sci. Eng., 61 (1999) 229-233, https://doi.org/10.1016/S0921-5107(98)00508-X

[52] Z.C. Feng, W.J. Choyke, J.A. Powell, Raman determination of layer stresses and strains for heterostructures and its application to the cubic SiC/Si system. J. Appl. Phys., 64(12) (1988) 6827-6835, https://doi.org/10.1063/1.341997

[53] S.I. Nakashima, H. Harima, Raman investigation of SiC polytypes. Phys. Status Solidi, 162(1) (1997) 39-64, https://doi.org/10.1002/1521-396X(199707)162:1<39::AID-PSSA39>3.0.CO;2-L

[54] M.J. Madito, T.T. Hlatshwayo, C.B. Mtshali, Chemical disorder of a-SiC layer induced in 6H-SiC by Cs and I ions co-implantation: Raman spectroscopy analysis. Appl. Surf. Sci., 538 (2021) 148099, https://doi.org/10.1016/j.apsusc.2020.148099

[55] L. Zhang, W. Jiang, C. Pan, R.C. Fadanelli, W. Ai, L. Chen, T. Wang, Raman study of amorphization in nanocrystalline 3C–SiC irradiated with C+ and He+ ions. J. Raman Spectrosc., 50(8) (2019) 1197-1204, https://doi.org/10.1002/jrs.5631

[56] D.N. Talwar, Probing optical, phonon, thermal and defect properties of 3C–SiC/Si

(001). Diam. Relat. Mater., 52 (2015) 1-10, https://doi.org/10.1016/j.diamond.2014.11.011

[57] H. Hobert, H. Dunken, R. Menzel, T. Bachmann, W. Wesch, Infrared and Raman spectroscopy of particle-beam induced damage of silicon carbide. J. Non. Cryst. Solids, 220(2-3) (1997) 187-194, https://doi.org/10.1016/S0022-3093(97)00305-0

[58] A. Perez-Rodriguez, Y. Pacaud, L. Calvo-Barrio, C. Serre, W. Skorupa, J.R. Morante, Analysis of ion beam induced damage and amorphization of 6H-SiC by Raman scattering. J. Electron. Mater., 25(3) (1996) 541-547, https://doi.org/10.1007/BF02666633

[59] W. Bolse, Formation and development of disordered networks in Si-based ceramics under ion bombardment. Nucl. Instrum. Methods Phys. Res B., 141(1-4) (1998) 133-139, https://doi.org/10.1016/S0168-583X(98)00086-X

[60] A. Zwick, R. Carles, Multiple-order Raman scattering in crystalline and amorphous silicon. Phys. Rev. B., 48(9) (1993) 6024, https://doi.org/10.1103/PhysRevB.48.6024

[61] M. Ehbrecht, H. Ferkel, F. Huisken, L. Holz, Y.N. Polivanov, V.V. Smirnov, O.M. Stelmakh, R. Schmidt, Deposition and analysis of silicon clusters generated by laser-induced gas phase reaction. J. Appl. Phys., 78(9) (1995) 5302-5306, https://doi.org/10.1063/1.360737

[62] J.C. Burton, L. Sun, M. Pophristic, S.J. Lukacs, F.H. Long, Z.C. Feng, I.T. Ferguson, Spatial characterization of doped SiC wafers by Raman spectroscopy. J. Appl. Phys., 84(11) (1998) 6268-6273, https://doi.org/10.1063/1.368947

[63] W. Bolse, J. Conrad, F. Harbsmeier, M. Borowski, T. Rödle, Long and short range order in ion irradiated ceramics studied by IBA, EXAFS and Raman. Mater. Sci. Forum, 248 (1997) 319-326, https://doi.org/10.4028/www.scientific.net/msf.248-249.319

[64] W. Bolse, J. Conrad, T. Rödle, T. Weber, Ion-beam-induced amorphization of 6H-SiC. Surf. Coat. Technol., 74 (1995) 927-931, https://doi.org/10.1016/0257-8972(95)08288-3

[65] Y. Yang, C. Zhang, C. Su, Z. Ding, Y. Song, Damage and recovery behavior of 4H-SiC implanted with He ions. Nucl. Instrum. Methods Phys. Res B., 449 (2019) 54-57, https://doi.org/10.1016/j.nimb.2019.04.055

[66] S. Sorieul, J.M. Costantini, L. Gosmain, L. Thomé, J.J. Grob, Raman spectroscopy study of heavy-ion-irradiated α-SiC. J. Phys. Condens. Matter, 18(22) (2006) 5235,

https://doi.org/10.1088/0953-8984/18/22/022

[67] X. Yuan, L.W. Hobbs, Modeling chemical and topological disorder in irradiation-amorphized silicon carbide. Nucl. Instrum. Methods Phys. Res. B., 191(1-4) (2002) 74-82, https://doi.org/10.1016/S0168-583X(02)00516-5

[68] K. Xue, L.S. Niu, Understanding the changes in mechanical properties due to the crystalline-to-amorphization transition in SiC. J. Appl. Phys., 106(8) (2009) 083505, https://doi.org/10.1063/1.3245391

[69] A. Zandiatashbar, G.H. Lee, S.J. An, S. Lee, N. Mathew, M. Terrones, T. Hayashi, C.R. Picu, J. Hone, N. Koratkar, Effect of defects on the intrinsic strength and stiffness of graphene. Nat. Commun., 5(1) (2014) 1-9, https://doi.org/10.1038/ncomms4186

[70] Z.A.Y. Abdalla, M.Y.A. Ismail, E.G. Njoroge, T.T. Hlatshwayo, E. Wendler, J.B. Malherbe, Migration behaviour of selenium implanted into polycrystalline 3C–SiC. Vac., 175 (2020) 109235, https://doi.org/10.1016/j.vacuum.2020.109235

[71] L.L. Snead, S.J. Zinkle, J.C. Hay, M.C. Osborne, Amorphization of SiC under ion and neutron irradiation. Nucl. Instrum. Methods Phys. Res B., 141(1-4) (1998) 123-132, https://doi.org/10.1016/S0168-583X(98)00085-8

[72] W.K. Burton, N. Cabrera, F.C. Frank, The growth of crystals and the equilibrium structure of their surfaces. Philos. trans. R. Soc. Lond., 243(866) (1951) 299-358, https://doi.org/10.1098/rsta.1951.0006

[73] S. Reboh, A.A.D. De Mattos, F. Schaurich, P.F.P. Fichtner, M.F., Beaufort, J.F. Barbot, The mechanisms of surface exfoliation in H and He implanted Si crystals. Scr. Mater., 65(12) (2011) 1045-1048, https://doi.org/10.1016/j.scriptamat.2011.09.012

[74] N. Daghbouj, J. Lin, H.S. Sen, M. Callisti, B. Li, M. Karlik, T. Polcar, Z. Shen, M. Zhou, T. You, and X. Ou. Blister formation in He-H co-implanted InP: A comprehensive atomistic study. Appl. Surf. Sci., 552 (2021), p.149426, https://doi.org/10.1016/j.apsusc.2021.149426

[75] N. Daghbouj, B.S. Li, M. Karlik, and A.J.A.S.S. Declemy. 6H-SiC blistering efficiency as a function of the hydrogen implantation fluence. Appl. Surf. Sci., 466 (2019), pp.141-150, https://doi.org/10.1016/j.apsusc.2018.10.005

[76] E. Friedland, N.G. van der Berg, J.B. Malherbe, E. Wendler, W. Wesch, Influence of radiation damage on strontium and iodine diffusion in silicon carbide. J. Nucl. Mater., 425(1-3) (2012) 205-210, https://doi.org/10.1016/j.jnucmat.2011.10.032

[77] F. Gao, W.J. Weber, M. Posselt, V. Belko, Atomistic study of intrinsic defect migration in 3C-SiC. Phys. Rev. B, 69(24) (2004) 245205,

https://doi.org/10.1103/PhysRevB.69.245205

[78] D. Sun, R. Li, J. Ding, P. Zhang, Y. Wang, J. Zhao, Interaction between helium and intrinsic point defects in 3C-SiC single crystal. J. Appl. Phys., 121(22) (2017) 225111, https://doi.org/10.1063/1.4985604

[79] F. Gao, W.J. Weber, M. Posselt, V. Belko, Atomic computer simulations of defect migration in 3C and 4H-SiC. Mater. Sci. Forum, 457 (2004) 457-460, https://doi.org/10.4028/www.scientific.net/MSF.457-460.457

[80] M. Bockstedte, A. Mattausch, O. Pankratov, Ab initio study of the annealing of vacancies and interstitials in cubic SiC: Vacancy-interstitial recombination and aggregation of carbon interstitials. Phys. Rev. B, 69(23) (2004) 235202, https://doi.org/10.1103/PhysRevB.69.235202

[81] H. Huang, N.M. Ghoniem, J.K. Wong, M. Baskes, Molecular dynamics determination of defect energetics in beta-SiC using three representative empirical potentials. Model. Simul. Mat. Sci. Eng., 3(5) (1995) 615, https://doi.org/10.1088/0965-0393/3/5/003